Journal of Materials Science: Materials in Engineering

ORIGINAL PAPER

Open Access

$CuMn_2O_4$ spinel electrodes: effect of the hydrothermal treatment duration on electrochemical performance

Souha Aouini[1*], Afrah Bardaoui[1], Ana M. Ferraria[2,3], Radhouane Chtourou[1] and Diogo M. F. Santos[4*]

Abstract

$CuMn_2O_4$ (CMO) thin films are produced using a simple hydrothermal method. The influence of reaction duration on the electrodes' electrochemical performance is investigated. XRD data shows improved crystal structure after 24-h reaction time, with a crystallite size of 12.17 nm. Distinct vibrational peaks associated with Cu–O and Mn–O are observed in the ATR-FTIR spectra, corroborating the spinel formation after 24 h. XPS analysis shows a compositional shift over time, starting with copper hydroxide at 12 h, evolving into a mix of copper and manganese oxides, hydroxides, and oxyhydroxides by 18 h, and achieving the desired spinel composition by 24 h. Microscopic analysis reveals CMO is arranged as small sheet structures, with 4.95 ± 2.92 µm in length after 24-h reaction. The CMO_{24h} electrode displays a maximum specific capacitance of 1187.50 Fg^{-1} at a scan rate of 1 mVs^{-1} in 1 M Na_2SO_4 electrolyte. The electrochemical performance of the synthesized CMO electrodes reveals a high potential for energy storage applications.

Keywords $CuMn_2O_4$ spinel, Energy storage, Hydrothermal reaction, Electrochemical properties, Specific capacitance

Introduction

Energy storage systems have emerged as a central focus of research and development, attracting significant attention for their indispensable role in diverse applications. The quest for effective energy storage solutions has led to the investigation of various technologies, including supercapacitors (SCs). SCs have garnered significant attention due to their quick rechargeability, superior power density relative to batteries, and enhanced storage capacity compared to conventional capacitors (Lu et al. 2017). In addition to combining the qualities of both traditional capacitors and batteries, SCs have a promising energy storage capacity. Electrochemical supercapacitors are grouped into three types based on how they store charges: hybrid capacitors, electrical double-layer capacitors (EDLCs), and pseudocapacitors (Forouzandeh et al. 2020). In contrast to the active electrodes found in EDLCs, which are made of carbon-based materials like activated carbon, graphene, and carbon nanotubes, pseudocapacitors are made of conducting polymers and different metal oxides. Another kind of SC is a hybrid capacitor, which combines EDLCs and pseudocapacitors (Miller et al. 2018). The active electrode materials used to build these kinds of SCs are created by fusing two or three different elements, giving them a much higher specific capacitance and greater energy density than EDLCs

*Correspondence:
Souha Aouini
souha.aouini@etudiant-fst.utm.tn
Diogo M. F. Santos
diogosantos@tecnico.ulisboa.pt
[1] Laboratory of Nanomaterials and Systems for Renewable Energies (LaNSER), Research and Technology Center of Energy (CRTEn), Techno-Park Borj Cedria, Bp 95, Hammam-Lif, 2050 Tunis, Tunisia
[2] BSIRG, iBB (Institute for Bioengineering and Biosciences), Chemical Engineering Department, Instituto Superior Técnico, Universidade de Lisboa, Lisbon 1049-001, Portugal
[3] Associate Laboratory i4HB — Institute for Health and Bioeconomy at Instituto Superior Técnico, Universidade de Lisboa, 1049-001 Lisbon, Portugal
[4] Laboratory for Physics of Materials and Emerging Technologies, Chemical Engineering Department, Center of Physics and Engineering of Advanced Materials, Instituto Superior Técnico, Universidade de Lisboa, 1049-001 Lisbon, Portugal

or pseudocapacitors (Chen et al. 2014). The limited lifespan in cyclic performance of conductive polymers, along with the relatively lower capacitance exhibited by carbon-based materials and the higher cost associated with typical noble metal oxides (e.g., ruthenium oxide, RuO_2), continue to pose significant challenges for all types of SCs (Borenstein et al. 2017; Yadav and Sharma 2021). RuO_2 is a promising material due to its excellent cycle stability and suitable specific capacitance, but ruthenium's scarcity and exorbitant prices are major drawbacks (Majumdar et al. 2019). Overcoming these limitations necessitates research into alternative materials for supercapacitor production (Soudan et al. 2002). Metal oxides, including mixed transition metal oxides (MTMOs), emerge as a promising alternative. These compounds are favored over single transition metal oxide components and exhibit enhanced chemical stability and superior electrochemical properties when utilized as electrode materials for supercapacitors. Moreover, they have showcased electrochemical performance on par with or surpassing RuO_2 (Yuan et al. 2014). In recent times, there has been significant research on various compounds, including metal oxides, metal sulfides, and binary transition metal oxides characterized by spinel structures like $CoMn_2O_4$ (Bhagwan et al. 2021; Aouini et al. 2022), $ZnMn_2O_4$ (Aouini et al. 2022), and $CuMn_2O_4$ (Cheng et al. 2022), and other types of electrode materials have gained prominence in supercapacitor research due to their notably high theoretical specific capacitance (Deka 2023). Within this category of oxides, considerable research has focused on manganese-based binary oxides, establishing them as prominent electrode materials. Manganese boasts several advantageous traits, including its low toxicity, widespread availability, multiple valences, and cost-effectiveness (Zhang et al. 2015; Dessie et al. 2019).

A few of the many applications for $CuMn_2O_4$ include photocatalysts (Aouini et al. 2022), lithium-ion batteries (Li et al. 2018), sensors (Cui et al. 2022), supercapacitors (Cheng et al. 2022; Zhang et al. 2021; Sheikhzadeh and Sanjabi 2021), and others (Gao et al. 2021; Guo et al. 2018; Ranjbar-Nouri et al. 2018). It can be produced through diverse methods, such as hydrothermal synthesis (Li et al. 2018), solid-state reaction (Vinod et al. 2018), sol–gel techniques (Wan et al. 2021), thermal decomposition (Afriani et al. 2018), spray pyrolysis (McCloy et al. 2012), reflux methods (Li et al. 2018), co-melting technique (Parida et al. 2016), and co-precipitation (John et al. 2019). Among the various nanostructure synthesis techniques, the hydrothermal approach is recognized for its capacity to create metal oxide nanoparticles. This method is known to yield nanoparticles with a stable microstructure and consistent composition at a cost-effective rate (Yang and Park 2019). Metal oxides like $CoMn_2O_4$ (Nassar and Abdallah 2016), $NiCo_2O_4$ (Liu et al. 2013), $NiFe_2O_4$ (Zhou et al. 2005), and $CuMn_2O_4$ have all been produced hydrothermally.

To the best of the authors' knowledge, this work reports for the first time an investigation into the impact of hydrothermal reaction duration on the structural, morphological, and electrochemical properties of synthesized $CuMn_2O_4$ (CMO) samples. The CMO thin films were produced over stainless steel mesh (SSM) through a simple, one-step hydrothermal process. During the synthesis, various reaction times (6, 12, 18, and 24 h) were employed to create distinct CMO electrodes. The electrochemical performance of these electrodes was then systematically evaluated in a Na_2SO_4 electrolyte to assess their potential as electrodes for energy storage applications.

Methods

Materials synthesis

All the required chemicals were obtained from Sigma-Aldrich for the synthesis. The method utilized in this process was hydrothermal synthesis, enabling the deposition of CMO spinels directly onto a stainless steel mesh (SSM). These SSM substrates, characterized by a wire diameter of 35 µm and an opening width of 45 µm, underwent precision cutting into rectangular segments measuring 2×5 cm^2. Subsequently, they were immersed in hydrochloric acid, subjected to a sequential cleaning process involving 10 min of treatment in an ultrasonic cleaner using a combination of acetone and ethanol, and finally rinsed with distilled water.

For sample preparation, aqueous solutions containing 0.075-M tetrahydrate copper chloride (II) and 0.15-M tetrahydrate manganese chloride (II) ($MnCl_2.4H_2O$) were formulated. These compounds were dissolved in 20 mL of distilled water in a 1:2 molar ratio while undergoing magnetic stirring at 800 rpm for 40 min. The resulting solution was titrated with 5-M sodium hydroxide (NaOH) until reaching a pH of 10. The reaction mixture was transferred to a Teflon-coated stainless steel autoclave and held at 180 °C for varying durations of 6, 12, 18, and 24 h. Subsequently, the coated substrate was delicately removed from the container and washed with distilled water. Finally, the SSM coated with the deposit underwent heating in a muffle furnace at 400 °C for 2 h under an air atmosphere.

Materials characterization

X-ray diffraction (XRD) measurements were conducted at room temperature utilizing CuKα radiation ($k = 1.541$ Å) and a Bruker system D8 advance X-ray diffractometer procured from Bruker Inc., headquartered in Billerica, MA, USA. The attenuated total reflection

— Fourier transform-infrared spectroscopy (ATR-FTIR) analysis was performed using a PerkinElmer Spectrum two FTIR spectrometer from Perkin Elmer Inc. in Waltham, MA, USA, equipped with a UATR-2 accessory. Spectral data were collected by conducting 32 scans at a resolution of 4 cm^{-1} in the transmission mode using PerkinElmer Spectrum IR software, all undertaken under typical room temperature conditions. A Kratos XSAM800 double anode spectrometer (Kratos Analytical Ltd., Manchester, UK) was used to conduct X-ray photoelectron spectroscopy (XPS). Both X-ray sources give rise to spectral superpositions: with Al Kα, Mn 2p, and Cu 2p are overlapping (at least partially) Cu LMM and Mn LMM, respectively; with Mg Kα, only Mn 2p has some degree of superposition with Mn LMM, and Cu 2p region does not coincide with any other relevant spectral feature. Therefore, the Mg Kα source ($h_v = 1253.6$ eV) was selected to irradiate the CMO samples. Additional operating conditions and data treatment details were published elsewhere (Aouini et al. 2022). The morphological analysis using scanning electron microscopy with energy-dispersive X-ray spectroscopy (SEM–EDS) involved utilizing a Hitachi S-2400 model by Hitachi Inc. in Tokyo, Japan, along with a Bruker light elements EDS detector from Bruker Inc. in Billerica, MA, USA. This analysis employed a focused electron beam operating at an energy level of 25 keV.

Electrochemical measurements

The electrodes' electrochemical properties were examined in a conventional three-electrode system using Squidstat Plus, an electrochemical workstation provided by Admiral Instruments (USA). The electrolyte was 1 M Na_2SO_4. The experimental setup involved utilizing the synthesized CMO materials as the working electrode, a platinum mesh as the counter electrode, and a HI5412 saturated calomel electrode (SCE, Hanna Instruments) as the reference. Electrochemical impedance spectroscopy (EIS) results were analyzed and fitted with ZView software from Scribner LLC (Southern Pines, NC, USA).

Results and discussion

Structural and morphological characterization

Structural study by X-ray diffraction (XRD)

The XRD diagrams in Fig. 1a illustrate the samples produced at varying hydrothermal duration from 6 to 24 h. The 6-h sample exhibited an amorphous nature and was excluded from further analysis. The 12-h and 18-h samples displayed a tetragonal crystal structure. Their lattice parameters were determined to be (a = b = 6.226 Å, c = 18.155 Å) and (a = b = 8.903 Å, c = 7.836 Å), respectively, which is consistent with standard reference cards (JCPDS 96–591-0242) for a tetragonal crystal system with space group I41/amd. The increase in reaction time to 24 h induced a crucial phase transition from tetragonal to cubic (matching cubic CMO reference: JCPDS

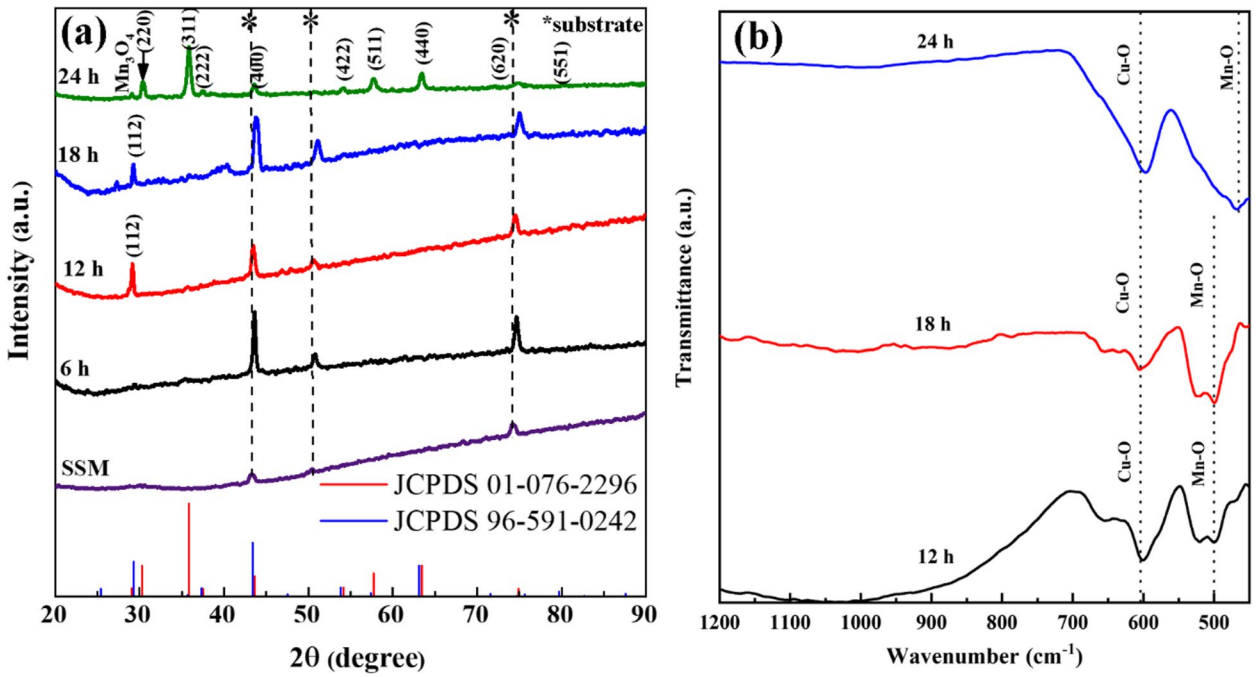

Fig. 1 **a** XRD patterns of CMO spinels on an SSM substrate acquired at varying hydrothermal durations from 6 to 24 h and **b** ATR-FTIR spectra of CMO spinels acquired at varying hydrothermal durations from 12 to 24 h

01–076-2296, space group $Fd\bar{3}m$ with a lattice constant of 8.300 Å), though a minor Mn_3O_4 secondary phase was also present. Based on the primary diffraction peaks, the average crystallite size for the 24-h sample was 12.17 nm by using the Scherrer equation (Eq. 1) (Scherrer 1918).

$$D = \frac{K\lambda}{\beta\cos\theta} \quad (1)$$

where D is the crystallite size, β is the FWHM in radians, $\lambda = 0.15406$ nm is the wavelength of the X-rays, θ is the Bragg angle, and K is the shape factor.

Microstrain (ε) and dislocation density (δ) were determined from Eqs. 2 and 3 (Williamson and Hall 1953).

$$\beta\cos\theta = \frac{K\lambda}{D} + 4\varepsilon\sin\theta \quad (2)$$

$$\delta = \frac{1}{D^2} \quad (3)$$

The analysis targeted the most prominent peak associated with the (311) plane, at a 2θ of 35.840° and a β-value of 0.488. A dislocation density of 8.140×10^{15} m^{-2} and micro-deformation of 0.169 were determined, in agreement with previous studies conducted on CMO (Parida et al. 2016; John et al. 2019).

ATR-FTIR spectroscopic analysis

The chemical bonding within the CMO structures was examined using ATR-FTIR spectroscopy (Fig. 1b), covering the 1200 to 400 cm^{-1} range for the synthesized samples at 12 h, 18 h, and 24 h. The spectra revealed a broad absorption band (733–1213 cm^{-1}) related to Mn–O–OH bond vibrations, losing strength with extended reaction time. Two consistent and broad bands (450–700 cm^{-1}) related to M–O (M = Cu or Mn) lattice vibrations were observed (Li et al. 2021; Ashourdan et al. 2021). Notably, the position of the Cu–O stretching vibration band (~ 600 cm^{-1}) did not shift across the reaction duration. However, the band exhibited a higher intensity at 24 h. For the Mn–O vibrational stretching modes, a clear distinction is observed in the positions of the bands: CMO_{12h} and CMO_{18h} exhibited two bands at ~ 500 and ~ 520 cm^{-1}, while CMO_{24h} presented a broader band at ~ 440 cm^{-1}. This shift towards lower wavenumbers in vibrational frequency is reasonably attributed to alterations in the manganese chemical structure, accompanied by corresponding crystallographic changes from a tetragonal to a cubic lattice structure, as evidenced by the XRD analysis.

Surface study by XPS

The XPS spectra are depicted in Fig. 2. The wide spectra (Fig. 2a) indicate the presence of Mn, Cu, and O, as well as C, without other impurities. The overall quantification is shown in Table 1, along with the experimental Mn/Cu and O_{metal}/Cu atomic ratios.

The main component of the Cu 2p doublet (Fig. 2b) was fitted with three primary peaks positioned at 930.7 ± 0.1 eV, 933.1 ± 0.3 eV, and 934.4 ± 0.3 eV. The Auger parameter (AP) (Cu $2p_{3/2}$, $L_3M_{45}M_{45}$) = 1848.3 ± 0.2 eV indicates that the peak centered at low-binding energy (BE) is assigned to Cu(I); the peak centered at 933.1 eV is attributed to Cu(II) oxide, as evidenced by the multiplet structure, detected roughly between 938 and 946 eV (Marques et al. 2008),and the peak at 934.4 eV is generally attributed to Cu(II) hydroxides (Marques et al. 2008).

Mn $2p_{3/2}$ region (Fig. 2c) was fitted with three main peaks, with the most intense centered at 641.3 ± 0.5 eV assigned to Mn(III). This oxidation state was further supported by the average distance ($\Delta = 5.5 \pm 0.2$ eV) between the Mn 3s photoelectron peak (~ 84 eV) and its multiplet (~ 89.6 eV) in 18-h and 24-h samples. Such a difference has been associated with manganese oxyhydroxide (Ilton et al. 2016). As observed for other Mn-based binary oxide spinel structures (Aouini et al. 2022; Aouini et al. 2023), the XPS Mn 2p region also revealed a peak at higher binding energy (643.0 ± 0.6 eV) assigned to Mn(IV), likely mixed with Mn in higher oxidation states. In the CMO_{24h} Mn $2p_{3/2}$ region, a fourth peak at 640.2 ± 0.1 eV was attributed to Mn(II), possibly indicating the presence of the secondary phase of Mn_3O_4, which corroborates the findings of the XRD analysis.

Moreover, from the analysis of both Cu 2p and Mn 2p regions, it is interesting to note that the detection of Cu(I) for longer times of synthesis seems to result from the reduction of part of the copper existing at the extreme surface with concomitant manganese oxidation. The increasing intensity of the Cu(I) peak follows the increase of the intensity of the Mn $2p_{3/2}$ at 645.5 eV, assigned to Mn(VII) (Biesinger et al. 2011). The inset in Fig. 2c shows the increasing chemical shift resulting from the oxidation of a fraction of Mn(III). These observations are compatible with the presence of $Cu(I)Mn(VII)O_4$ and $Cu(I)Mn(III)Mn(IV)O_4$ at the surface. Clearly, the XPS overall results indicate mixed valences for Cu and Mn species in the synthesized CMO, consistent with spinel-like characteristics.

The O 1s region in Fig. 2d exhibited two fitted peaks at 529.8 ± 0.1 eV and 531.2 ± 0.1 eV, assigned to oxygen in the O^{2-} spinel structure and oxygen from metal hydroxides, respectively. Peaks with higher binding energy in the O 1s region correspond to oxidized carbonaceous groups (Hantsche 1993). In the C 1s region (Fig. 2e), three identified peaks at 285.0 ± 0.1 eV, 286.6 ± 0.1 eV, and 288.6 ± 0.1 eV correspond to C–C or C–H sp^3, C–O, and O–C = O, respectively.

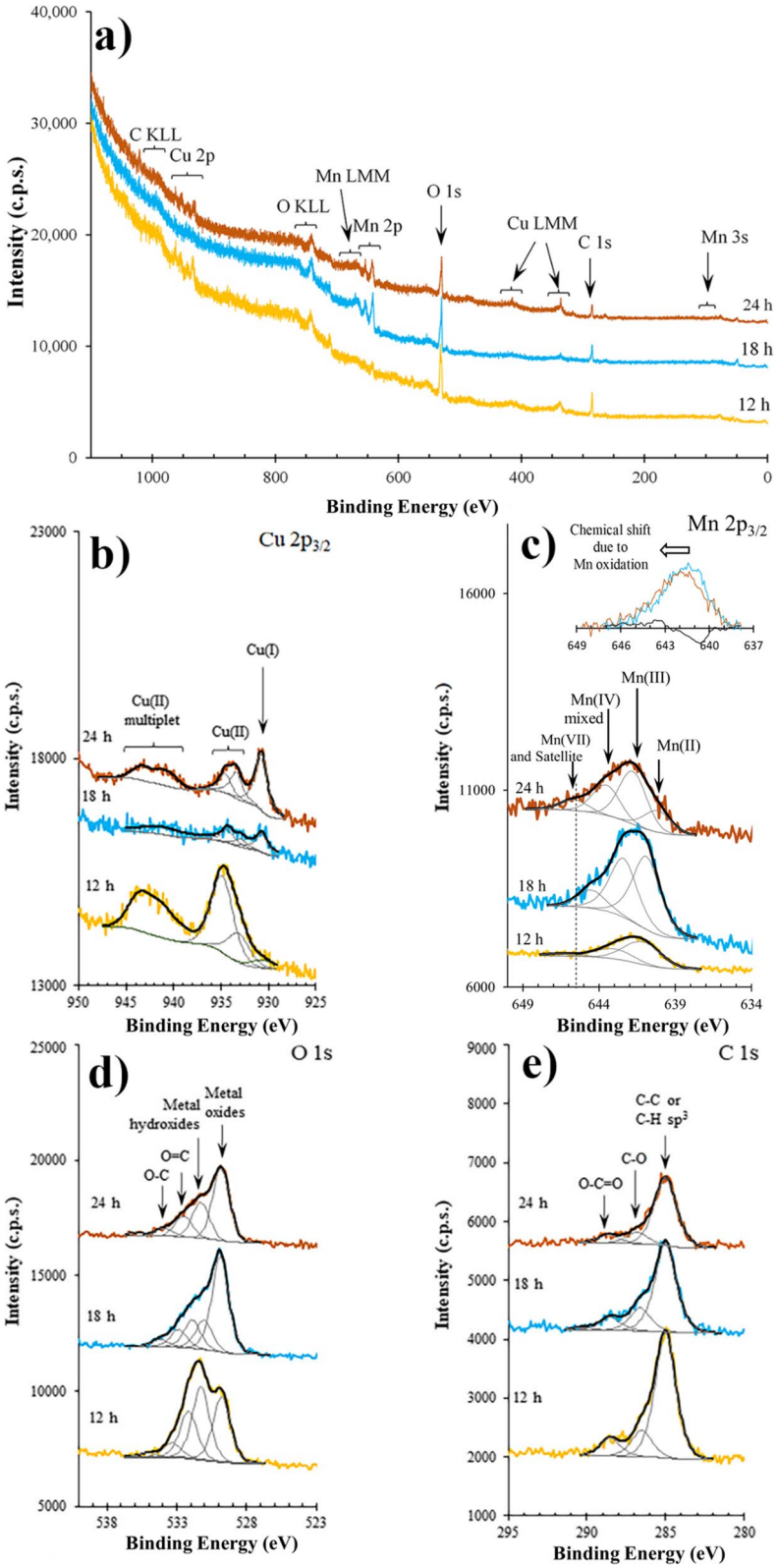

Fig. 2 **a** Survey XPS spectra of CMO spinels acquired at varying hydrothermal method durations from 12 to 24 h and XPS regions of **b** Cu $2p_{3/2}$, **c** Mn $2p_{3/2}$, **d** O 1s, and **e** C 1s of CMO spinels acquired at varying hydrothermal durations from 12 to 24 h. Peaks fitted in Cu 2p multiplet region are not included for clarity's sake. The inset in Mn $2p_{3/2}$ shows the peak shift towards higher BEs due to Mn oxidation from 18 to 24 h. The black line is the spectra difference [Mn $2p_{(24\,h)}$–Mn $2p_{(18\,h)}$], obtained after background subtraction and spectra normalization to the area of the CMO_{18h}

Table 1 Atomic concentrations (at.%) and atomic ratios in the synthesized CMO spinels. "O_{metal}" only includes oxygen bonded to manganese and copper (oxides and hydroxides)

	12 h	18 h	24 h
at.%			
C	38.8	35.1	32.3
O	48.0	47.2	47.3
Cu	9.5	3.2	6.9
Mn	3.7	14.5	13.5
Atomic ratios			
Mn/Cu	0.4	4.5	1.9
O_{metal}/Cu	2.6	10.3	4.6

In the predicted CMO spinel structure, Mn/Cu is expected to be close to 2. However, the experimental Mn/Cu atomic ratios in Table 1 show a Mn/Cu < 1 for CMO_{12h}, indicating a surface Mn depletion, while CMO_{18h} exhibits Mn/Cu > > 2, indicating a Mn excess. The CMO_{12h} spectrum notably differs from other samples (Fig. 2a), suggesting a surface primarily composed of copper hydroxides, indicated by prominent peaks in Cu $2p_{3/2}$ (most intense peak at 934.9 eV) and O 1 s (most intense peak at 531.3 eV) regions. CMO_{12h} also contains a residual amount of chlorine (1 at.%, not included in Table 1 quantification), likely from unreacted precursor. After 18 h of hydrothermal treatment, the surface composition shifts, with copper hydroxides no longer predominant, replaced by a mixture of copper and manganese oxides and oxyhydroxides. The Mn/Cu = 4.5 in CMO_{18h} may result from varying attenuation effects induced by the carbon overlayer. Mn 2p photoelectrons, having higher kinetic energy than Cu 2p photoelectrons, are more attenuated, leading to these observed ratios. CMO_{24h}, with slightly less carbon or a different surface distribution, approaches atomic ratios found in the $CuMn_2O_4$ spinel structure, consistent with the preceding XRD analysis.

Morphological study by SEM–EDS

Figure 3 depicts the morphology of CMO samples prepared at different reaction durations, ranging from 12 to 24 h. SEM images of the 12-h sample reveal irregular, flat sheet-like nanostructures on the substrate, with varying sizes and shapes. A nonuniform structure is also present. The 18-h sample exhibits a similar morphology, characterized by a partially nonuniform structure and microflat sheets. These observations align with XPS and ATR-FTIR analyses, indicating the presence of hydroxides and oxyhydroxides at 12 and 18 h.

For the 24-h sample, a sheet-like structure with a larger particle size is observed. The reduction of the nonuniform structures in the CMO_{24h} sample is likely due to the decrease of hydroxides and carbon in the material, coupled with the formation of the desired cubic spinel structure. XRD and ATR-FTIR analyses corroborate this transformation, showing the transition to a cubic structure during the 24-h hydrothermal treatment.

The average particle dimensions were obtained from Fig. 3 utilizing ImageJ software. The microsheets of the CMO_{24h} sample had an average length of 4.59 ± 2.92 µm. Figure 3d, h, and l presents the EDS spectra of the synthesized samples, confirming the presence of Cu, Mn, and O in all three samples. Ni, Fe, and Cr were also detected in low concentrations, originating from the stainless steel mesh (SSM). Chloride was also identified in the 12-h sample, possibly due to unreacted precursors, consistent with the XPS analysis findings. The EDS analysis reveals elemental ratios, with Mn/Cu values of 0.93, 2.41, and 1.75 for the 12-h, 18-h, and 24-h samples, respectively. Based on these findings, it is evident that the duration of the hydrothermal process plays a crucial role in forming the CMO structure. Longer reaction times allow for improved crystal growth and organization, leading to the development of the predicted spinel structure with well-defined sheet morphology.

Electrochemical characterization

Capacitance measurements

The electrochemical performance and specific capacitance of CMO electrodes were determined using cyclic voltammetry (CV) characterization. The cyclic voltammetry curves of CMO produced at 12 h, 18 h, and 24 h, shown in Fig. 4, were measured at different scan rates ranging from 1 to 100 mV s^{-1} within a constant potential window ranging from 0.2 to 0.6 V. The shape of CV curves shows a quasi-rectangular shape, revealing the capacitive behavior of the material (Kavinkumar et al. 2019). The symmetrical shape of the curve implies that the system exhibits good electrochemical reversibility. It suggests that the charge transfer occurs equally efficiently in both directions during the electrochemical process (Ray et al. 2019). Increasing scan rates lead to a corresponding increase in current density, while the shape of the CV curves remains consistent. This behavior indicates that the material retains good stability and demonstrates positive electrochemical performance (Du et al. 2009). Additionally, Fig. 4 shows a significant rise in the currents from the CVs of CMO_{12h} to those of CMO_{18h}, followed by an outstanding increase for CMO_{24h}, with the currents almost doubling their value.

The integral of the cyclic voltammetry curves was employed to calculate the system's capacitance, C_s, following Eq. 4:

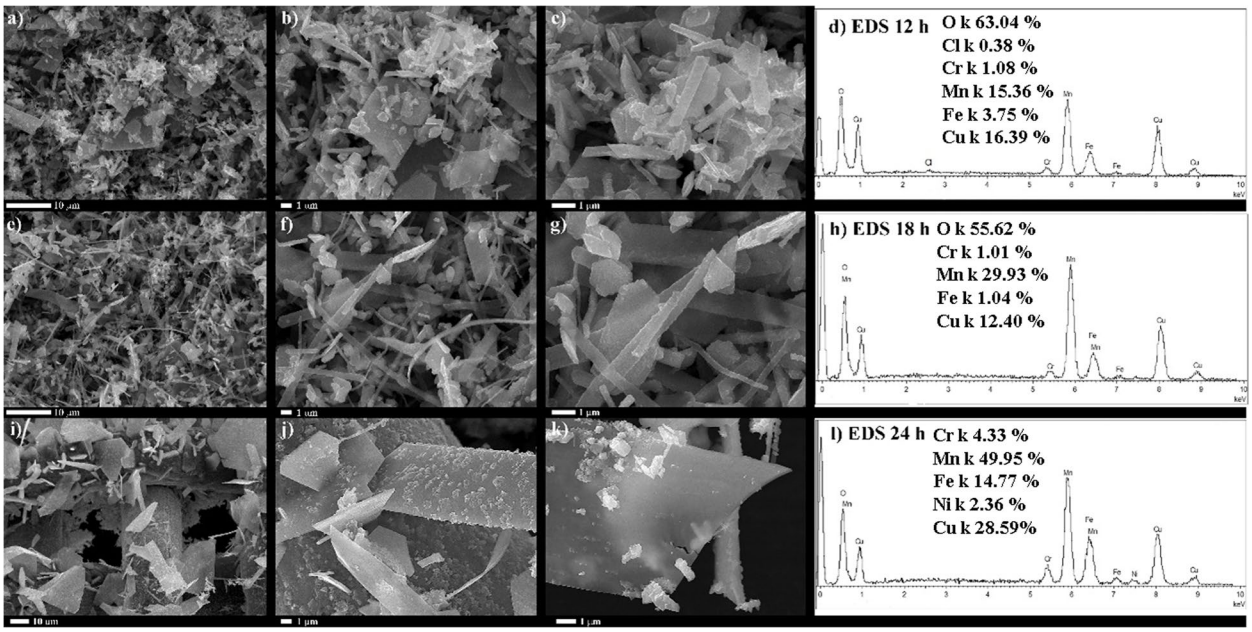

Fig. 3 SEM images of CMO spinels acquired during **a**, **b**, **c** 12 h, **e**, **f**, **g** 18 h, and **i**, **j**, **k** 24 h and the corresponding EDS spectra showing Cu, Mn, and O in CMO spinels obtained during **d** 12 h, **h** 18 h, and **l** 24 h

$$C_s = \frac{\int IdV}{2m\nu\Delta V} \tag{4}$$

where the numerator of the equation represents the total area under the CV curve, ΔV is the selected potential window (V), ν is the scan rate (mV s^{-1}), and m is the active material mass (g).

Table 2 shows how specific capacitance changes with different hydrothermal reaction durations. The capacitance increased from 540.15 F g^{-1} for the CMO_{12h} sample to 551.19 F g^{-1} for the CMO_{18h} sample. The CMO synthesized for 24 h exhibited the highest specific capacitance, reaching a value of 1181.50 F g^{-1}. Increasing the reaction duration to 24 h reduces the amount of amorphous particles, leading to improved capacitance due to the formation of the predicted spinel structure. The purity of the material thus influences the changes in specific capacitance with the hydrothermal reaction duration. The highest capacitance for each material was obtained at a scan rate of 1 mV s^{-1}. However, ions have ample time to diffuse throughout the electrode pores at slower scan rates, enabling complete insertion reactions and maximizing capacitance. However, as scan rates increase, the interaction time between ions and

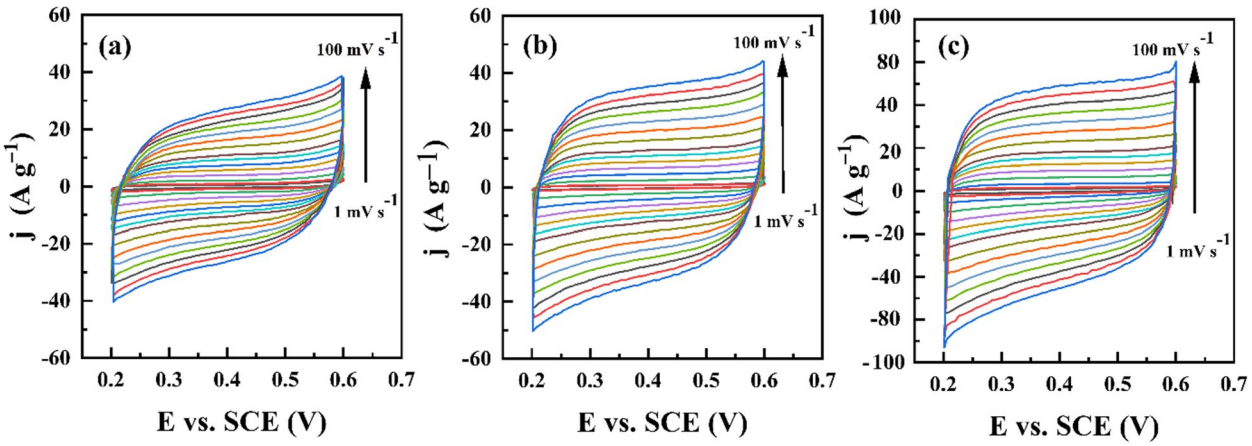

Fig. 4 The impact of scan rate (1–100 mV s^{-1}) on the cyclic voltammetry (CV) curves of CMO spinels synthesized at **a** 12 h, **b** 18 h, and **c** 24 h

Table 2 Specific capacitance of CMO spinels measured at various scan rates

Scan rate (mV s^{-1})	Specific capacitance (F g^{-1})		
	12 h	18 h	24 h
1	540.15	551.19	1181.5
2	477.09	307.92	1003.4
5	409.32	451.04	944.33
10	372.09	424.70	905.30
15	358.98	422.50	826.80
20	344.81	414.36	786.25
25	338.31	407.33	736.99
30	326.48	394.53	697.86
40	306.41	377.75	679.79
50	286.26	359.59	664.09
60	274.87	346.01	640.10
70	263.10	335.37	624.03
80	254.03	326.14	615.53
90	246.53	317.66	604.37
100	238.59	310.91	593.39

the electrode surface is limited, resulting in incomplete insertion and decreased measured capacitance (Aouini et al. 2022).

Galvanostatic cycling

To better understand the capacitive nature of the synthesized CMO particles, galvanostatic cycling studies were also carried out at different specific currents (5, 6, 7, 8, 9 A g^{-1}) in a potential window from 0.2 to 0.6 V (Fig. 5). From Fig. 5a, b, and c, it is noticeable that the discharge duration is lower than the charge time in the galvanostatic charge/discharge (GCD) curves obtained at a low specific current (5 A g^{-1}) because of the slow diffusion of electrolyte ions within the spinel; therefore, it takes a long time to activate all components (Saravanakumar et al. 2017). Comparing the three synthesized samples (Fig. 5d), it is clear that CMO_{24h} has the longest discharge time.

The estimated specific capacitance, C_s, of the three synthesized CMO samples may also be calculated from Eq. 5, where I is the current in amperes and Δt is the discharge time in seconds. Figure 5e and Table 3 show the obtained results.

$$C_s = \frac{I\Delta t}{m\Delta V} \tag{5}$$

The comparative analysis of specific capacitance across materials synthesized at 12, 18, and 24 h reveals that an extended hydrothermal duration results in superior capacitance. The 24-h sample reached a specific capacitance of 1011.87 F g^{-1} at a specific current of 5 A g^{-1}. This

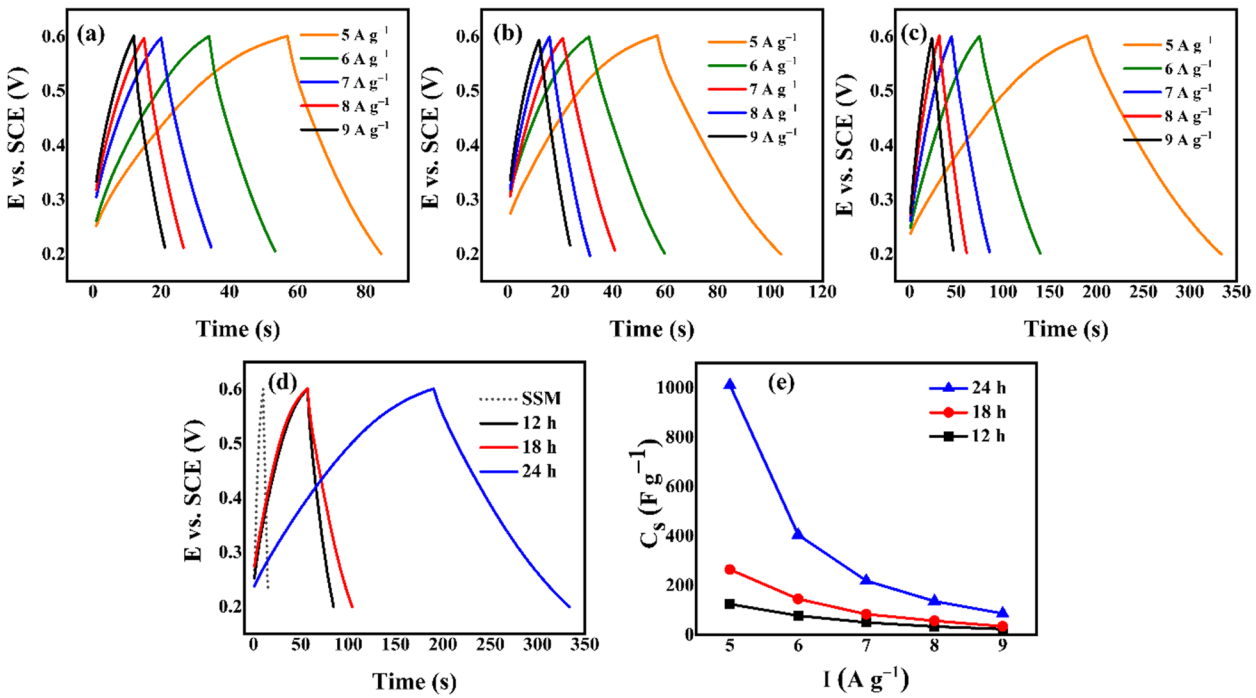

Fig. 5 Effect of specific current on GCD curves for CMO spinels obtained at **a** 12 h, **b** 18 h, and **c** 24 h. **d** GCD curves at 5 A g^{-1} for CMO spinels (12 h, 18 h, 24 h) and bare SSM. **e** Specific capacitance variation in CMO spinels vs. specific current

Table 3 Specific capacitance of CMO spinels measured at different current densities from GCD plots

	Specific capacitance (F g^{-1})		
Current (A g^{-1})	12 h	18 h	24 h
5	123.97	264.4	1011.9
6	77.55	145	405.01
7	50	83.12	218.75
8	33.67	56.25	135.94
9	22.95	34.37	85.94

observation aligns with CV results obtained at 1 mV s^{-1}. The enhanced capacitance is attributed to the controlled and uniform morphology of CMO particles formed during the prolonged hydrothermal process.

Electrochemical impedance spectroscopy (EIS)

Electrochemical impedance spectroscopy (EIS) was performed on the CMO particles in an AC field (10 mV) applied with a frequency ranging from 1000 kHz to 1 Hz. Generally, in supercapacitors, the standard EIS response typically manifests as a semicircular curve due to the impedance of the series resistance and charge transfer, along with a Warburg resistance in the low-frequency range (Sheikhzadeh and Sanjabi 2021). Figure 6 shows the EIS study for CMO_{12h}, CMO_{18h}, and CMO_{24h}, revealing distinct charge transfer resistances, represented as R_{ct}. These variations in R_{ct} values can be attributed to differences in morphology, as evident from the SEM micrographs, and the contrasting crystal structures, as elucidated by XRD analyses.

The R_{ct} values of the materials produced for 12, 18, and 24 h are 92.7, 6.14, and 5.83 Ω, respectively. The CMO_{24h} sample displays a significantly lower R_{ct} value.

An equivalent circuit model has been constructed based on the experimental results, illustrated in Fig. 6c. This model integrates essential elements, such as the series resistance, R_s, charge transfer resistance, R_{ct}, and the constant phase element, CPE, Warburg diffusion resistance, W. The values of each parameter obtained from the fitting of the three samples' Nyquist plots can be seen in Table 4. The double-layer capacitance, C_{dl}, was determined using Eq. 6:

$$C_{dl} = \frac{1}{2\pi Z_{img} m} \tag{6}$$

where Z_{img} represents the imaginary part of the impedance. Figure 6d shows the C_{dl} vs. frequency curve. The comparison of the three materials shows that the sample product at 24 h has the highest double-layer capacitance.

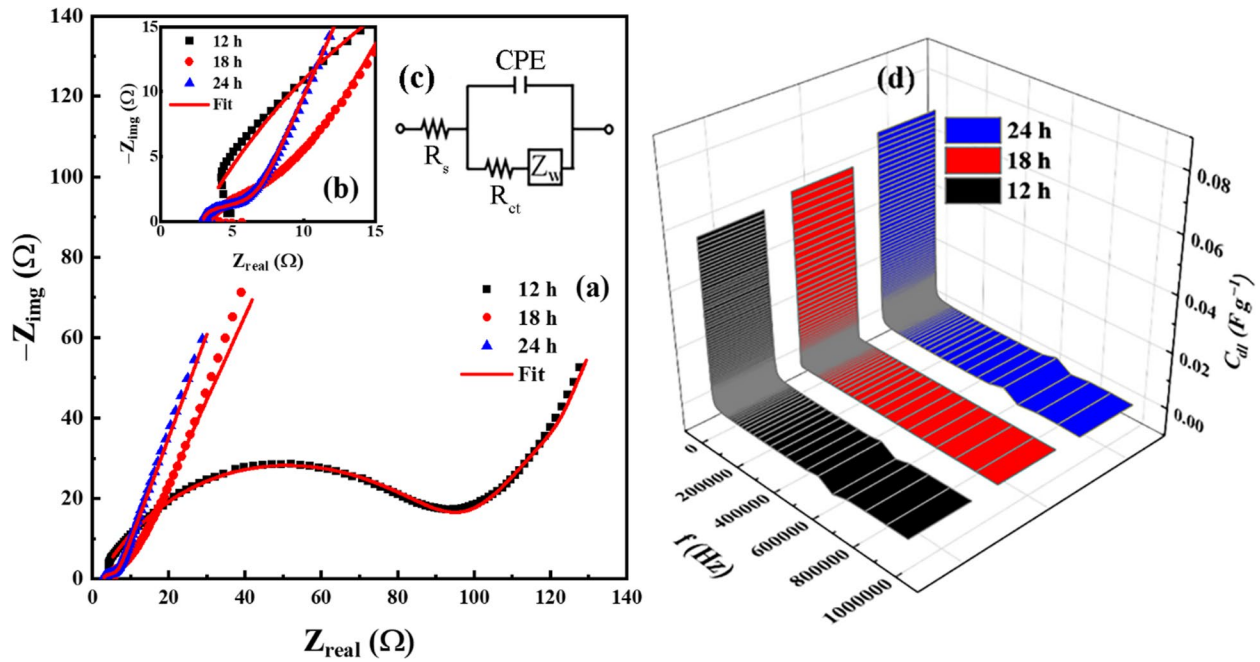

Fig. 6 **a** Nyquist plots for CMO spinels at 12, 18, and 24 h, **b** high-frequency region zoomed-in Nyquist plots, **c** equivalent circuit model, and **d** specific double-layer capacitance plots for CMO spinels generated at 12 h, 18 h, and 24 h vs. frequency

Table 4 Equivalent circuit parameters for CMO spinels obtained at 12, 18, and 24 h

Sample	R_s (Ω)	CPE		R_{ct} (Ω)	Z_W (Ω)	χ^2
		Y_0 (*S*)	n_{CPE}			
12 h	2.0	7.9×10^{-6}	0.68	92.7	187.7	5.69×10^{-4}
18 h	3.3	5.4×10^{-5}	0.74	6.14	17.5	8.26×10^{-4}
24 h	3.0	2.2×10^{-6}	0.98	5.83	7.4	8.44×10^{-4}

Conclusions

This work explored the influence of hydrothermal reaction duration on the physicochemical, morphological, and electrochemical characteristics of synthesized spinel manganites. The XRD data confirmed improved crystallinity after 24 h of reaction time, yielding a crystallite size of 12.17 nm. The ATR-FTIR spectra exhibit distinctive vibrational peaks characteristic of the spinel phase. XPS shows that the surface composition evolves with the treatment time, being a mixture of copper and manganese oxides, hydroxides, and/or oxyhydroxides at lower hydrothermal reaction durations. After 24 h of hydrothermal treatment, the predominant metal oxidation states Cu(II) and Mn(III) coexist with Cu(I), Mn(IV), and Mn(VII), indicating surface-level reduction of copper and oxidation of manganese. The experimental XPS atomic ratios attest that the CMO spinel stoichiometry is reached for the CMO_{24h} sample. CMO spinels were presented as microsheets with a length of 4.95 ± 2.92 µm after 24 h of hydrothermal process. EDS showed Mn/Cu and O/Cu ratios consistent with theoretical stoichiometric values. The electrochemical evaluation of the produced materials confirms that CMO_{24h} exhibits the highest specific capacitance, confirming its best energy storage features. These results are in good agreement with the assessed structural and morphological properties. The results indicate that the 24-h copper spinel manganites are promising energy storage materials, as evidenced by the electrochemical results.

Authors' contributions

SA contributed to conceptualization, formal analysis, investigation, and the initial drafting of the manuscript. AMF provided substantial input for formal analysis (XPS) and investigation. Both DMFS and AMF contributed valuable insights through critical review and manuscript editing. DMFS, AB, and RC gave supervisory guidance. All authors have reviewed and endorsed the final version of the manuscript for publication.

Funding

This study received funding from the Tunisian Ministry of Higher Education and Scientific Research and from Fundação para a Ciência e a Tecnologia (FCT, Portugal) through research unit grants to iBB (UIDB/04565/2020, UIDP/04565/2020) and i4HB (LA/P/0140/2020). A. M. F. acknowledges Instituto Superior Técnico for the Scientific Employment contract IST-ID/131/2018. Additionally, appreciation is extended to FCT and CeFEMA for the research contract as part of programmatic funding (UIDP/04540/2020) (D. M. F. S.).

Availability of data and materials

The data supporting this study's findings are available on request from the corresponding author.

Declarations

Competing interests

The authors declare that they have no competing interests.

Received: 5 April 2024 Accepted: 3 July 2024
Published online: 11 July 2024

References

Afriani F, Ciswandi A, Hermanto B, Sudiro T (2018) Synthesis of $CuMn_2O_4$ spinel and its magnetic properties characterization. AIP Confer Proc 1964:020016

Aouini S, Bardaoui A, Ferraria A, Santos D, Chtourou R (2022) $ZnMn_2O_4$ nanopyramids fabrication by hydrothermal route: effect of reaction time on the structural, morphological, and electrochemical properties. Energies (basel) 15:9352. https://doi.org/10.3390/en15249352

Aouini S, Bardaoui A, Santos DMF, Chtourou R (2022) Hydrothermal synthesis of $CuMn_2O_4$ spinel-coated stainless steel mesh as a supercapacitor electrode. J Mater Sci: Mater Electr 33:12726–12733. https://doi.org/10.1007/s10854-022-08219-4

Aouini S, Bardaoui A, do Rego AMB, Ferraria AM, Santos DMF, Chtourou R (2023) Synthesis and characterization of $CoMn_2O_4$ spinel onto flexible stainless-steel mesh for supercapacitor application. Solid State Sci 143:107283. https://doi.org/10.1016/j.solidstatesciences.2023.107283

Ashourdan M, Semnani A, Hasanpour F, Moosavifard SE (2021) Synthesis of $CuMnO_2$/graphene quantum dot nanocomposites as novel electrode materials for high performance supercapacitors. J Energy Storage 36:102449. https://doi.org/10.1016/j.est.2021.102449

Bhagwan J, Krishna BNV, Yu JS (2021) Template and sol-gel routed $comn_{2o4}$ nanofibers for supercapacitor applications. Int J Energy Res 45:19413–19422. https://doi.org/10.1002/er.7096

Biesinger MC, Payne BP, Grosvenor AP, Lau LWM, Gerson AR, Smart RSTC (2011) Resolving surface chemical states in XPS analysis of first row transition metals, oxides and hydroxides: Cr, Mn, Fe Co and Ni. Appl Surf Sci 257:2717–2730. https://doi.org/10.1016/j.apsusc.2010.10.051

Borenstein A, Hanna O, Attias R, Luski S, Brousse T, Aurbach D (2017) Carbon-based composite materials for supercapacitor electrodes: a review. J Mater Chem A Mater 5:12653–12672. https://doi.org/10.1039/C7TA00863E

Chen LY, Hou Y, Kang JL, Hirata A, Chen MW (2014) Asymmetric metal oxide pseudocapacitors advanced by three-dimensional nanoporous metal electrodes. J Mater Chem A Mater 2:8448. https://doi.org/10.1039/c4ta00965g

Cheng C, Cheng Y, Lai G (2022) $CuMn_2O_4$ hierarchical microspheres as remarkable electrode of supercapacitors. Mater Lett 317:132102. https://doi.org/10.1016/j.matlet.2022.132102

Cui Q, Zhang W, Wang T, Zhang C, Wang W, Wang J, Wang S, Yang P, Xu H (2022) Highly sensitive non-enzymatic glucose sensor based on $cumn_2o_4$

shuttles supporting on Ni foam. Ionics (kiel) 28:2447–2456. https://doi.org/10.1007/s11581-022-04459-w
Deka S (2023) Nanostructured mixed transition metal oxide spinels for supercapacitor applications. Dalton Trans 52:839–856. https://doi.org/10.1039/D2DT02733J
Dessie Y, Tadesse S, Eswaramoorthy R, Abebe B (2019) Recent developments in manganese oxide based nanomaterials with oxygen reduction reaction functionalities for energy conversion and storage applications: a review. J Sci: Adv Mater Devices 4:353–369. https://doi.org/10.1016/j.jsamd.2019.07.001
Du X, Wang C, Chen M, Jiao Y, Wang J (2009) Electrochemical performances of nanoparticle Fe_3O_4 / activated carbon supercapacitor using KOH electrolyte solution. J Phys Chem C 113:2643–2646. https://doi.org/10.1021/jp8088269
Forouzandeh P, Kumaravel V, Pillai SC (2020) Electrode materials for supercapacitors: a review of recent advances. Catalysts 10:969. https://doi.org/10.3390/catal10090969
Gao Y, Li B, Zhang Z, Zhang X, Deng Z, Huo L, Gao S (2021) $CuMn_2O_4$ spinel nanoflakes for amperometric detection of hydrogen peroxide. ACS Appl Nano Mater 4:6832–6843. https://doi.org/10.1021/acsanm.1c00898
Guo Y, Song Z, Xu B, Li Y, Qi F, Croue J-P, Yuan D (2018) A novel catalytic ceramic membrane fabricated with $CuMn_2O_4$ particles for emerging UV absorbers degradation from aqueous and membrane fouling elimination. J Hazard Mater 344:1229–1239. https://doi.org/10.1016/j.jhazmat.2017.11.044
Hantsche H. High resolution XPS of organic polymers, the Scienta ESCA300 Database. G. Beamson and D. Briggs eds. Wiley: Chichester 1992;295 Pp., Hardcover, £ 65.00, ISBN 0–471–93592–1. Advanced Materials 1993;5:778–778. https://doi.org/10.1002/adma.19930051035.
Ilton ES, Post JE, Heaney PJ, Ling FT, Kerisit SN (2016) XPS determination of Mn oxidation states in Mn (Hydr)oxides. Appl Surf Sci 366:475–485. https://doi.org/10.1016/j.apsusc.2015.12.159
John AM, Pramothkumar A, Senthilkumar N, Jothivenkatachalam K, Fermi Hilbert IP, Joseph PJ (2019) Flake-like $CuMn_2O_4$ nanoparticles synthesized via co-precipitation method for photocatalytic activity. Physica B Condens Matter 572:117–124. https://doi.org/10.1016/j.physb.2019.07.047
Kavinkumar V, Verma A, Masilamani S, Kumar S, Jothivenkatachalam K, Fu Y-P (2019) Investigation of the structural, optical and crystallographic properties of Bi_2WO_6/Ag plasmonic hybrids and their photocatalytic and electron transfer characteristics. Dalton Trans 48:10235–10250. https://doi.org/10.1039/C9DT01807G
Li L, Jiang G, Ma J (2018) $CuMn_2O_4$/graphene nanosheets as excellent anode for lithium-ion battery. Mater Res Bull 104:53–59. https://doi.org/10.1016/j.materresbull.2018.03.051
Li A, Liu Y, Wang Z, Song Z, Zhang Y, Wang Y, Xu B, Qi F, Ikhlaq A, Kumirska J et al (2021) Catalytic ozonation membrane reactor integrated with $CuMn_2O_4$/RGO for degradation emerging UV absorbers (BP-4) and fouling in-situ self-cleaning. Sep Purif Technol 279:119804. https://doi.org/10.1016/j.seppur.2021.119804
Liu Z-Q, Xu Q-Z, Wang J-Y, Li N, Guo S-H, Su Y-Z, Wang H-J, Zhang J-H, Chen S (2013) Facile hydrothermal synthesis of urchin-like $NiCo_2O_4$ spheres as efficient electrocatalysts for oxygen reduction reaction. Int J Hydrogen Energy 38:6657–6662. https://doi.org/10.1016/j.ijhydene.2013.03.092
Lu Y, Li B, Zheng S, Xu Y, Xue H, Pang H (2017) Syntheses and energy storage applications of $M_x S_y$ (M = Cu, Ag, Au) and their composites: rechargeable batteries and supercapacitors. Adv Funct Mater 27:1703949. https://doi.org/10.1002/adfm.201703949
Majumdar D, Maiyalagan T, Jiang Z (2019) Recent progress in ruthenium oxide-based composites for supercapacitor applications. ChemElectroChem 6:4343–4372. https://doi.org/10.1002/celc.201900668
Marques MT, Ferraria AM, Correia JB, do Rego AMB, Vilar R (2008) XRD, XPS and SEM characterisation of Cu–NbC nanocomposite produced by mechanical alloying. Mater Chem Phys 109:174–180
McCloy JS, Leslie C, Kaspar T, Jiang W, Bordia RK (2012) Magnetic behavior of Ni and Co doped $CuMn_2O_4$ spinels. J Appl Phys 111:07E149. https://doi.org/10.1063/1.3680530
Miller EE, Hua Y, Tezel FH (2018) Materials for energy storage: review of electrode materials and methods of increasing capacitance for supercapacitors. J Energy Storage 20:30–40. https://doi.org/10.1016/j.est.2018.08.009
Nassar MY, Abdallah S (2016) Facile controllable hydrothermal route for a porous $CoMn_2O_4$ nanostructure: synthesis, characterization, and textile dye removal from aqueous media. RSC Adv 6:84050–84067. https://doi.org/10.1039/C6RA12424K
Parida SK, Mohapatra J, Mishra DK (2016) Structural and magnetic behavior of spinel $CuMn_2O_4$ synthesized by co-melting technique. Mater Lett 181:116–118. https://doi.org/10.1016/j.matlet.2016.05.180
Ranjbar-Nouri Z, Soltanieh M, Rastegari S (2018) Applying the protective $CuMn_2O_4$ spinel coating on AISI-430 ferritic stainless steel used as solid oxide fuel cell interconnects. Surf Coat Technol 334:365–372. https://doi.org/10.1016/j.surfcoat.2017.11.036
Ray A, Roy A, Ghosh M, Alberto Ramos-Ramón J, Saha S, Pal U, Bhattacharya SK, Das S (2019) Study on charge storage mechanism in working electrodes fabricated by sol-gel derived spinel $NiMn_2O_4$ nanoparticles for supercapacitor application. Appl Surf Sci 463:513–525. https://doi.org/10.1016/j.apsusc.2018.08.259
Saravanakumar B, Muthu Lakshmi S, Ravi G, Ganesh V, Sakunthala A, Yuvakkumar R (2017) Electrochemical properties of rice-like copper manganese oxide ($CuMn_2O_4$) nanoparticles for pseudocapacitor applications. J Alloys Compd 723:115–122. https://doi.org/10.1016/j.jallcom.2017.06.249
Scherrer P (1918) Estimation of the size and internal structure of colloidal particles by means of Röntgen. Nachr Ges Wiss Göttingen 2:96–100
Sheikhzadeh M, Sanjabi S (2021) Coelectrodeposition of crystalline copper-manganese oxide containing $CuMn_2O_4$ spinel for high energy supercapacitor application. Synth Met 278:116802. https://doi.org/10.1016/j.synthmet.2021.116802
Soudan P, Gaudet J, Guay D, Bélanger D, Schulz R (2002) Electrochemical properties of ruthenium-based nanocrystalline materials as electrodes for supercapacitors. Chem Mater 14:1210–1215. https://doi.org/10.1021/cm010721c
Vinod K, Satya AT, Ravindran NR, Mani A (2018) Magnetic and magnetocaloric properties of $CuMn_2O_4$ and Mn_3O_4 composite system. Mater Res Express 5:056104. https://doi.org/10.1088/2053-1591/aac1ec
Wan X, Tang N, Xie Q, Zhao S, Zhou C, Dai Y, Yang Y (2021) A $CuMn_2O_4$ spinel oxide as a superior catalyst for the aerobic oxidation of 5-hydroxymethylfurfural toward 2,5-furandicarboxylic acid in aqueous solvent. Catal Sci Technol 11:1497–1509. https://doi.org/10.1039/D0CY01649G
Williamson GK, Hall W (1953) X-ray line broadening from filed Al and W. Acta Metal 1:22–31
Yadav S, Sharma A (2021) Importance and challenges of hydrothermal technique for synthesis of transition metal oxides and composites as supercapacitor electrode materials. J Energy Storage 44:103295. https://doi.org/10.1016/j.est.2021.103295
Yang G, Park S-J (2019) Conventional and microwave hydrothermal synthesis and application of functional materials: a review. Materials 12:1177. https://doi.org/10.3390/ma12071177
Yuan C, Wu HB, Xie Y, Lou XWD (2014) Mixed transition-metal oxides: design, synthesis, and energy-related applications. Angewandte Chemie Int Ed 53:1488–1504. https://doi.org/10.1002/anie.201303971
Zhang K, Han X, Hu Z, Zhang X, Tao Z, Chen J (2015) Nanostructured Mn-based oxides for electrochemical energy storage and conversion. Chem Soc Rev 44:699–728. https://doi.org/10.1039/C4CS00218K
Zhang C, Xie A, Zhang W, Chang J, Liu C, Gu L, Duo X, Pan F, Luo S (2021) $CuMn_2O_4$ spinel anchored on graphene nanosheets as a novel electrode material for supercapacitor. J Energy Storage 34:102181. https://doi.org/10.1016/j.est.2020.102181
Zhou J, Ma J, Sun C, Xie L, Zhao Z, Tian H, Wang Y, Tao J, Zhu X (2005) Low-temperature synthesis of $NiFe_2O_4$ by a hydrothermal method. J Am Ceram Soc 88:3535–3537. https://doi.org/10.1111/j.1551-2916.2005.00629.x

Publisher's Note